

# Magneto-optical trap for metastable helium at 389 nm

J.C.J. Koelemeij,\* R.J.W. Stas, W. Hogervorst, and W. Vassen

*Laser Centre Vrije Universiteit, De Boelelaan 1081, 1081 HV Amsterdam, The Netherlands*

(Dated: October 30, 2018)

We have constructed a magneto-optical trap (MOT) for metastable triplet helium atoms utilizing the  $2\ ^3S_1 \rightarrow 3\ ^3P_2$  line at 389 nm as the trapping and cooling transition. The far-red-detuned MOT (detuning  $\Delta = -41$  MHz) typically contains few times  $10^7$  atoms at a relatively high ( $\sim 10^9\text{ cm}^{-3}$ ) density, which is a consequence of the large momentum transfer per photon at 389 nm and a small two-body loss rate coefficient ( $2 \times 10^{-10}\text{ cm}^3/\text{s} < \beta < 1.0 \times 10^{-9}\text{ cm}^3/\text{s}$ ). The two-body loss rate is more than five times smaller than in a MOT on the commonly used  $2\ ^3S_1 \rightarrow 2\ ^3P_2$  line at 1083 nm. Furthermore, we measure a temperature of 0.46(1) mK, a factor 2.5 lower as compared to the 1083 nm case. Decreasing the detuning to  $\Delta = -9$  MHz results in a cloud temperature as low as 0.25(1) mK, at small number of trapped atoms. The 389 nm MOT exhibits small losses due to two-photon ionization, which have been investigated as well.

PACS numbers: 32.80.Pj, 34.50.Fa, 34.50.Rk

## I. INTRODUCTION

A magneto-optical trap (MOT) is a standard tool in the production of cold atomic gases, allowing investigation of cold-collision phenomena [1] as well as the realization of Bose-Einstein condensation (BEC) in alkali species [2] and, more recently, in metastable triplet helium ( $\text{He}^*$ ) [3, 4].  $\text{He}^*$  has a high (19.8 eV) internal energy, which allows for real-time diagnostics and increased sensitivity in BEC probing. Unfortunately, the high internal energy also introduces strong Penning ionization losses in magneto-optically trapped atomic clouds, which imposes limits on the maximum achievable density. The two-body loss rate coefficient related to this process is about  $5 \times 10^{-9}\text{ cm}^3/\text{s}$  for a MOT on the  $2\ ^3S_1 \rightarrow 2\ ^3P_2$  transition at 1083 nm [5], which is about two orders of magnitude larger than the loss rate coefficient in a standard alkali MOT. In BEC experiments, the MOT is used as a bright source of cold atoms to load a magnetic trap with large numbers of atoms. Moreover, as a starting point for evaporative cooling a dense magnetostatically trapped cloud is desired. So ideally, the magneto-optically trapped cloud must provide this high density. In the present work, we explore the feasibility and possible advantages of a MOT using the  $2\ ^3S_1 \rightarrow 3\ ^3P_2$  transition at 389 nm for metastable helium, in comparison with the conventional  $2\ ^3S_1 \rightarrow 2\ ^3P_2$  (1083 nm) magneto-optical trap.

Although the 389 nm transition was used recently in laser cooling experiments [6], it has not found wide application yet. This mainly relates to the fact that 10% of the  $3\ ^3P_2$  population decays via the  $3\ ^3S_1$  state (Fig. 1), making a closed laser cooling transition between magnetic substates impossible. In addition, the shorter 389 nm wavelength leads, in combination with a linewidth  $\Gamma/2\pi = 1.5$  MHz [7], to a relatively high

saturation intensity  $I_0 = 3.31\text{ mW}/\text{cm}^2$  (circular polarization in an optically pumped environment [8]). In comparison, the  $2\ ^3S_1 \rightarrow 2\ ^3P_2$  transition at 1083 nm has almost the same linewidth but a saturation intensity of only  $0.17\text{ mW}/\text{cm}^2$ . To maximize the number of trapped atoms, dedicated metastable helium magneto-optical traps are operated at large detuning and intensity [5, 9, 10]. This implies the need for a high-power laser setup. Nevertheless, the concept of a 389 nm magneto-optical trap is appealing. An attractive feature of the 389 nm transition is the momentum transfer per photon, which is 2.8 times larger than for 1083 nm photons. Since both transitions have nearly equal linewidths, the spontaneous cooling force increases proportional to the photon momentum. This opens the possibility to compress the cloud substantially in comparison to a 1083 nm MOT at the same detuning and power. Unfortunately, compression may lead to increased losses predominantly due to light-assisted two-body collisions. The two-body loss rate coefficient for the 389 nm situation is, however, unknown. In case of a relatively low rate coefficient, the cloud may be compressed without loss of too many metastables. Furthermore, it should be noted that the 1083 nm and 389 nm transitions are electronically alike, which greatly facilitates the comparison between the two MOT types. Finally, the 389 nm MOT differs from the 1083 nm MOT in yet another respect: two 389 nm photons contain sufficient energy to ionize an atom in the  $2\ ^3S_1$  state. This may introduce observable additional losses.

In this article, we report on the study of a prototype 389 nm MOT. In Sec. II we present some typical aspects of the 389 nm MOT from general laser cooling theory. Next, we outline our experimental setup in Sec. III. Results are given in Sec. IV. Conclusive remarks and an outlook are presented in Sec. V.

---

\*Electronic address: koel@nat.vu.nl

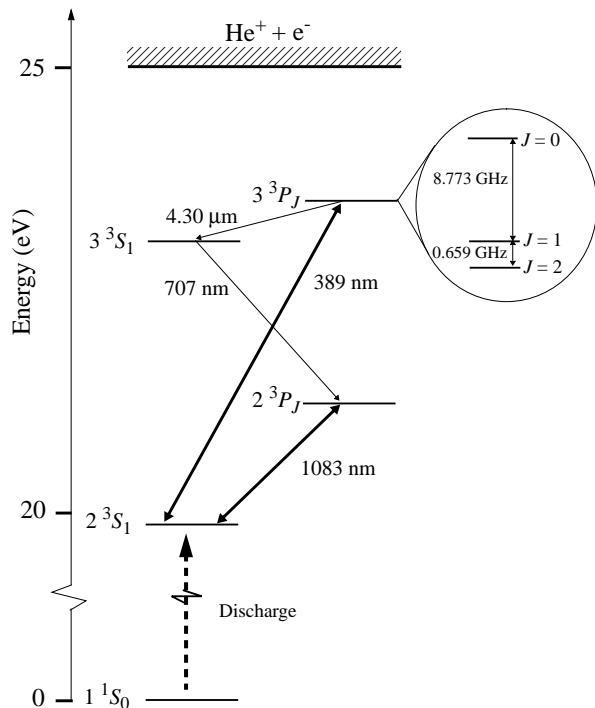


FIG. 1: Helium level scheme. The long-lived  $2^3S_1$  metastable state is populated in a DC discharge. The  $2^3S_1 \rightarrow 3^3P_2$  (389 nm) and  $2^3S_1 \rightarrow 3^3P_1$  (1083 nm) laser cooling transitions are indicated with bold arrows.

## II. QUALITATIVE DESCRIPTION OF THE 389 NM MOT

### A. Spring constant and damping coefficient

The large Doppler cooling force modifies the equilibrium conditions in a 389 nm MOT with respect to the 1083 nm situation. This follows from regarding the motion of an atom, trapped in a one-dimensional MOT, as an overdamped harmonic oscillation [11, 12]. The oscillation frequency  $\omega_{osc}$  and damping coefficient  $\epsilon_d$  are, for small velocities and small deviations from trap center, given by

$$\omega_{osc}^2 = 4\hbar k \frac{4\delta S \zeta}{m(1 + 2S + 4\delta^2)^2}, \quad (1)$$

$$\epsilon_d = 4\hbar k^2 \frac{4\delta S}{m(1 + 2S + 4\delta^2)^2}, \quad (2)$$

with  $k$  the wavenumber of the MOT laser light,  $m$  the atomic mass,  $\delta = 2\pi\Delta/\Gamma$  with  $\Delta$  the laser detuning from resonance in MHz,  $S = I/I_0$  the saturation parameter, with  $I$  the intensity per MOT beam, and  $\zeta$  representing the spatial derivative of the location-dependent Zeeman detuning. The harmonic oscillator frequency is related to the spring constant  $\kappa$  via  $\omega_{osc}^2 = \kappa/m$ . Two general differences between the 389 nm and 1083 nm MOT follow immediately from Eq. (1) and Eq. (2). First, bearing in mind that  $k_{389} = k_{1083} \times 1083/389$ , it is obvious that

for equal saturation parameter and detuning the damping coefficient increases by a factor 7.8 as compared to a 1083 nm MOT. Although this does not alter the temperature in the MOT, which does not depend on wavelength and is expected to be almost equal for the two cases, the damping time  $\tau$  is shortened to  $0.13\tau_{1083}$  [11]. Second, and under the same assumptions for the MOT parameters, the spring constant is increased by a factor 2.8. This has implications for the size of the trapped cloud, which is determined by the equipartition of potential and kinetic energy. The volume  $V$  of the cloud is (following the definition of  $V$  as given in Sec. III C 2)

$$V = \left( \frac{2\pi k_B T}{\kappa} \right)^{3/2}, \quad (3)$$

where for simplicity we have assumed an isotropic 3D harmonic oscillator ( $k_B$  is Boltzmann's constant). It follows that the volume decreases by a factor 4.5, i.e. the cloud is compressed with respect to the 1083 nm situation.

### B. Loading the MOT

All magnetic substates participate in the atom-laser interaction, since the magneto-optically trapped cloud is contained at low magnetic field strengths and irradiated from six directions with circularly polarized light. Therefore, the presence of the second decay channel of the  $3^3P_2$  state will not limit operation of the MOT, as long as there is loading of atoms from the outer regions of the MOT volume. Loading, however, may be frustrated by the nonclosed cycling transition as well as by the relatively large Doppler shift. More specifically, the question arises whether the slowing process of atoms entering the MOT volume can be completed before a spontaneous emission via the  $3^3S_1$  cascade takes the atom to a different, nonresonant magnetic substate. If not, the atom needs to be repumped to the cycling transition; otherwise it will escape from the MOT volume. In order to answer this question, and to obtain a general notion of the loading process and its dependence on the MOT parameters, we employ a simple 1D model for an atom traversing the MOT volume. We calculate the instantaneous photon scattering rate for atoms at a given velocity  $v$ , interacting with a counterpropagating, red-detuned laser beam at 389 nm inducing  $\sigma^+$  transitions. This laser beam represents the two MOT laser beams counterpropagating the atomic beam at angles of  $\pm 45^\circ$  with respect to the atomic beam (see Sec. III A). We assume the atoms to be predecelerated by a Zeeman slower, so that we can choose any initial velocity. We take Zeeman detuning, laser intensity, and Doppler shift into account, the latter of which is taken to be  $kv/\sqrt{2}$  to correct for the  $\pm 45^\circ$  angle between the atom and (real) laser beams. Furthermore, we consider all three  $\sigma^+$  transitions, i.e.  $M = -1, 0, +1 \rightarrow M' = 0, +1, +2$  (of which

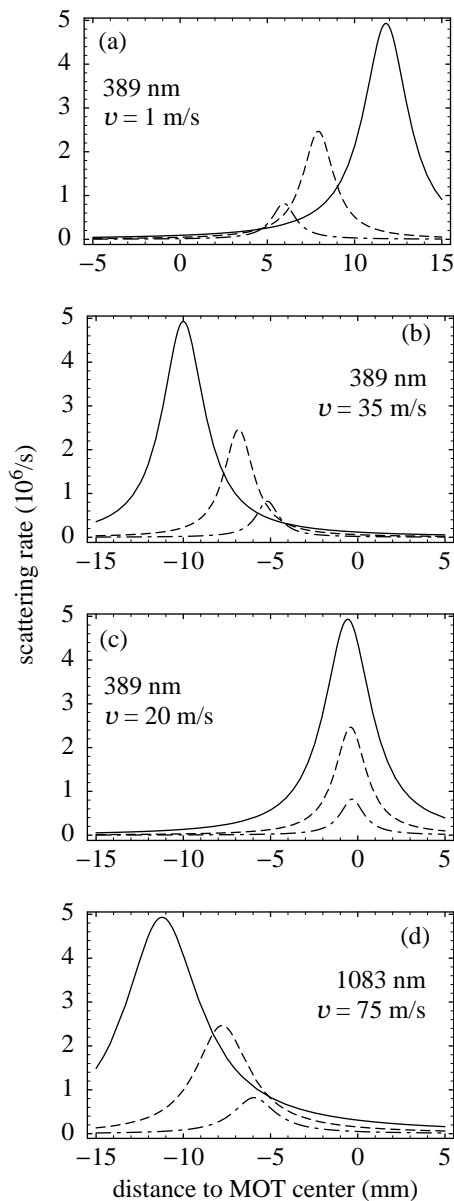


FIG. 2: (a)-(c) 389 nm and (d) 1083 nm photon scattering rates as a function of distance from the MOT center for  $M = 1 \rightarrow M' = 2$  (solid line),  $M = 0 \rightarrow M' = 1$  (dashed line), and  $M = -1 \rightarrow M' = 0$  (dash-dotted line) transitions.

the  $M = +1 \rightarrow M' = +2$  will be referred to as the laser cooling or cycling transition). In Fig. 2, plots are shown of the photon scattering rate for the three  $\sigma^+$  transitions as a function of the distance from the center of the MOT, measured along the symmetry axis of the Zeeman decelerator. The MOT light boundaries are at about  $\pm 10$  mm from the MOT center (see also Sec. III B), and the atoms are moving into the positive direction. Figure 2a shows the familiar behavior of the scattering force in a MOT. An atom, moving into the positive direction at a typical intra-MOT velocity  $v = 1$  m/s, scatters an increasing number of photons from the counterpropagating MOT

laser beam as it moves farther away from the MOT center. Consequently, it will be slowed down and eventually pushed back towards the center.

First, we use this model to investigate the capture of atoms, emerging from the Zeeman slower in the  $2^3S_1, M = +1$  state with a velocity  $v = 75$  m/s. We choose a MOT detuning of  $-35$  MHz, an intensity of  $30I_0$ , and a magnetic field gradient of  $20$  G/cm. These conditions are typical for a  $1083$  nm MOT. The model shows that the resonance condition is never fulfilled inside the MOT volume, thus preventing any loading of atoms. Next, we lower  $v$  to  $35$  m/s. We observe that the atoms now interact strongly with the laser light within the MOT volume (see Fig. 2b). However, the peaks in the scattering rate of the different  $\sigma^+$  transitions hardly overlap in space, as a result of their different Zeeman detunings. Slowing these atoms down to zero velocity requires about 190 absorption-emission cycles, whereas it takes about 20 cycles (corresponding to a velocity reduction of only 4 m/s) for the atom to end up in one of the nonabsorbing ( $M = -1$  or  $M = 0$ ) states. Consequently, the capture process is interrupted. Before this  $M$ -state atom becomes sufficiently resonant again, such that it is optically pumped back to the  $M = +1$  state, it will have travelled out of resonance with the cycling transition and can no longer be captured by the MOT. Only for velocities  $v \leq 20$  m/s, an atom ending up in the wrong  $M$  state is repumped fast enough to continue the deceleration towards zero velocity (Fig. 2c). Thus we conclude that the capture velocity of the  $389$  nm MOT is approximately 24 m/s. This velocity is much smaller than the  $\sim 75$  m/s capture velocity of a typical  $1083$  nm MOT. Figure 2d illustrates the superior loading capabilities of a  $1083$  nm MOT of 15 mm radius. The smaller Doppler shift allows for faster atoms to be captured, whereas the closed cycling transition does not impose any constraints on the magnetic field strength. In fact, the  $1083$  nm MOT diameter sets the maximum stopping distance, and thus limits the capture velocity. Within the picture provided by the model, increasing the diameter of a  $389$  nm MOT will not solve the problem described above. To avoid optical pumping to nonresonant magnetic substates in the outer regions of the MOT, only small magnetic field gradients can be tolerated. Then, to maintain sufficient confinement of the trapped atoms, only small MOT laser detunings are allowed, thereby limiting the capture velocity. We stress that the model is based on crude simplifications and ignores important features of the MOT. For instance, the orthogonal MOT laser beams, in combination with the spatially varying, three-dimensional magnetic field vector induce  $\sigma$  as well as  $\pi$  transitions. Therefore, the conditions required for repumping to the laser-cooled state may be less stringent than predicted by our simple model. So we conclude that a  $389$  nm MOT will be able to capture sufficiently slow metastable helium atoms.

The smaller capture velocity of a  $389$  nm MOT is a significant limitation, since a helium atomic beam expands dramatically due to transverse heating during Zee-

man deceleration [13]. Calculations of the rms size of the atomic beam along the slowing trajectory show an increase of the rms atomic beam diameter by a factor 1.7 when tuning the end velocity from 75 m/s down to 25 m/s. This may lead to a decrease of a factor 3 in metastable flux. In conjunction with the limited MOT volume, this inevitably will result in a reduced loading rate.

### III. EXPERIMENTAL SETUP

#### A. Atomic beam apparatus

The first stage in our atomic beam apparatus involves a liquid nitrogen cooled He\* DC discharge source, producing an atomic beam that is laser collimated using the curved-wavefront technique. The beam source is a copy of the source described by Rooijackers *et al.* [14]. The collimated beam enters a differentially pumped two-part Zeeman slower that reduces the longitudinal velocity from 1000 m/s to  $\sim 25$  m/s. 1083 nm laser light from a commercial 2W fiber laser (measured bandwidth 8 MHz) is used for slowing and collimation. The laser is stabilized to the  $2^3S_1 \rightarrow 2^3P_2$  transition using saturated absorption spectroscopy in an rf-discharge cell. The  $-250$  MHz detuning for Zeeman slowing is obtained using an acousto-optical modulator. Downstream the Zeeman slower the MOT vacuum chamber is located, with 20 mm diameter laser windows for the MOT beams (see Fig.3). Two channeltron electron multipliers are mounted inside to separately detect ions and metastables. Both channeltrons are operated with negative high voltage at the front end; however, one of them is put more closely to the cloud, thereby attracting all positively charged particles and leaving only the neutral metastables to be detected by the other. Also, the detector of metastables is hidden behind an aperture in the wall of the vacuum chamber (Fig. 3), which provides additional shielding of its electric field. Two 50 A coils, wound around the vacuum chamber and consisting of 17 turns copper tubing each, produce a quadrupole magnetic field with a gradient of 43 G/cm along the symmetry axis. The field of the second part of the Zeeman slower inside the MOT region is counteracted with a compensation coil, mounted at the position of the Zeeman slower exit. The pressure in the MOT chamber is  $2 \times 10^{-9}$  mbar, and increases to  $1 \times 10^{-8}$  mbar when the He\* beam is switched on.

To minimize atomic beam expansion at the end of the Zeeman slower, we overlap the Zeeman slower laser beam with an additional 1083 nm beam, with identical circular polarization and similar intensity, but different detuning ( $\Delta = -80$  MHz). By choosing the same sign of the quadrupole magnetic field gradient along the Zeeman slower axis as that of the Zeeman slower itself, an auxiliary Zeeman slowing stage only centimeters upstream of the MOT volume is established. This should allow

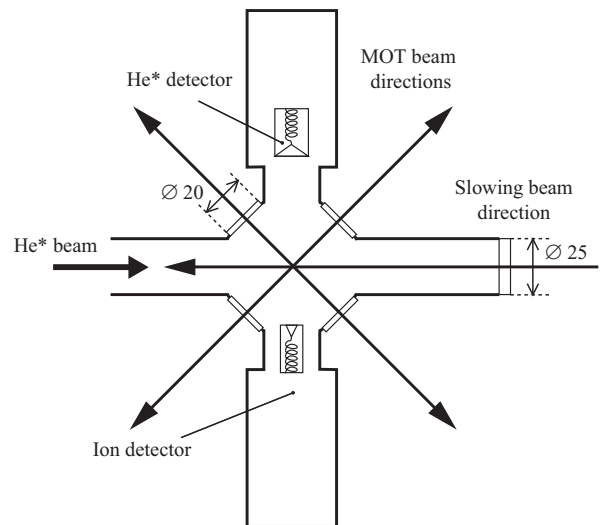


FIG. 3: Top view of the MOT vacuum chamber. Not shown are the vertical MOT laser beams. Dimensions are given in mm.

trapping of atoms with velocities up to 75 m/s at the end of the Zeeman slower. A calculation of the atomic beam diameter for this case indicates that the loading rate may be increased by a factor 2.4 compared to the case where the Zeeman slower decelerates atoms to a velocity of 24 m/s.

#### B. 389 nm Laser setup

The MOT laser light is obtained by frequency doubling the output of a Coherent 899 Titanium:sapphire (Ti:Sa) laser (778 nm with few-hundred kHz bandwidth) in an enhancement cavity containing a 10 mm Brewster-cut LBO crystal. The cavity length is locked to the fundamental wavelength using the Hänsch-Couillaud scheme. The Ti:Sa laser is pumped by 10 W at 532 nm from a Spectra-Physics Millennia X laser. We routinely produce 700 mW of 389 nm light; peak values of over 1 W of 389 nm at 2.1 W fundamental power have been achieved. We measured 4% short-term ( $\sim 10$  ms) power fluctuations in the 389 nm output [15]. The LBO crystal is flushed with oxygen, which increases the output power by about 10%. A small portion of the UV output is used to stabilize the wavelength to the  $2^3S_1 \rightarrow 3^3P_2$  transition with saturated absorption spectroscopy, while Zeeman-tuning the Lamb dip allows continuous adjustment of the detuning between 0 and  $\pm 230$  MHz. A combination of cylindrical and spherical lenses transforms the UV beam into a round, parallel and approximately Gaussian beam with 8 mm waist. The beam profile is truncated by a 20 mm circular aperture, followed by a series of nonpolarizing beamsplitters that split the UV beam into four beams. The individual beam intensities are chosen such that two beams in the horizontal plane can be retroreflected,

while the intensity of the two vertical beams along the symmetry axis of the quadrupole field ensures a more or less spherical He\* cloud.

### C. MOT diagnostics

#### 1. Time-of-flight measurement

The internal energy of helium metastables can be exploited in measuring time-of-flight (TOF) spectra of a MOT. Electron multipliers directly detect part of the expanding cloud after the atoms in the MOT have been released by suddenly switching off the MOT laser, the magnetic coils, and the slower beams. In our experiment, operating the channeltrons in current mode yields TOF signals resembling a Maxwell-Boltzmann atomic velocity distribution, from which we can deduce the temperature and number of trapped atoms in the cloud. However, this procedure requires knowledge of the channeltron gain which varies with the rate of detected particles and obscures the shape of the TOF spectrum to an unknown extent. To circumvent an elaborate calibration procedure, we count the individual metastables that hit the channeltron. This is, using a properly set amplifier/discriminator, not dependent on the momentary gain. The output of the amplifier/discriminator is subsequently integrated by a calibrated ratemeter. In this way we obtain the total number of detected metastables during the TOF. Knowing the solid angle covered by the detection area, the accuracy in the number of trapped atoms is now determined by the detection efficiency of a low-velocity triplet helium atom, which is estimated to be in the range 10–70% (see also Refs. [5, 14], and references therein). This measuring method therefore cannot provide better than 50% accuracy in the number of trapped atoms.

#### 2. Fluorescence detection

In addition to the determination of the MOT atom number by time-of-flight measurements, we monitor the fluorescence of the cloud using a calibrated CCD camera to independently determine the number of atoms. Here, the cascade via the  $3\ ^3S_1$  state offers the 706 nm wavelength, which is far more efficiently detected by a camera than fluorescence from a 1083 nm MOT. Moreover, the 706 nm light does not suffer from reabsorption, because of the insignificant population of the  $2\ ^3P_2$  level. Therefore we can safely assume the monitored fluorescence to be proportional to the number of atoms at each point in the cloud image, even at the highest densities obtained in our MOT. To calibrate the camera, we use a small fraction of the Ti:Sa laser output, with the laser tuned to 706 nm. In the atom number determination we use dichroic mirrors to block all other wavelengths scattered from the MOT, most importantly the abundant 389 nm light. To

extract the number of atoms  $N$  from the observed fluorescence power  $P_{fluor}$  we use the empirical equation of Townsend *et al.* [16], that relates the emitted power to the number of atoms:

$$P_{fluor} = N\hbar\omega \frac{\Gamma}{2} \frac{6CS}{1 + 6CS + 4\delta^2}. \quad (4)$$

In the above equation,  $S = I/I_0$ , where  $I_0$  is the saturation intensity in the case of  $\sigma^+$  transitions in an optically pumped environment, and  $I$  is the laser intensity of a single MOT beam. The phenomenological factor  $C$  incorporates the effects of reduced saturation; as the six circularly polarized MOT laser beams traverse the cloud in different directions and at varying angles with the quadrupole magnetic field, all transitions between the ground- and excited-state Zeeman levels must be considered, and the saturation intensity  $I_0$ , as defined above, no longer applies. It is pointed out in Ref. [16] that  $C$  lies somewhere halfway the average of the squared Clebsch-Gordan coefficients of all involved transitions, and 1. For the  $2\ ^3S_1 \rightarrow 3\ ^3P_2$  389 nm transition, the average of the squares of the Clebsch-Gordan coefficients is 0.56. Therefore, we adopt  $C = 0.8 \pm 0.2$ , as also chosen by Browaeys *et al.* [9]. This value incorporates a realistic estimate and an uncertainty that covers the range of all physically possible values of  $C$ .

The fluorescence image of the cloud is also used to determine the volume of the cloud. From a fit to a Gaussian distribution, we obtain the rms size in the radial ( $\sigma_\rho$ ) and axial ( $\sigma_z$ ) directions, and the volume  $V = (2\pi)^{3/2}\sigma_\rho^2\sigma_z$  ( $V$  contains 68% of the atoms). For a cloud with Gaussian density distribution, this definition of  $V$  conveniently connects the number of atoms  $N$  to the central density  $n_0$  via  $N = n_0V$ . This provides all necessary information to deduce the density distribution  $n(\mathbf{r})$ .

#### 3. Ion detection

In the MOT vacuum chamber, positive ions are produced in Penning-ionizing collisions of a He\* atom with another He\* atom or with a background gas molecule. These ions are subsequently attracted to and detected by the second channeltron, and the resulting output current provides a rough measure of the number of trapped atoms. This signal is particularly useful for optimization purposes. Moreover, the signal is used to monitor the trap decay after the loading of the MOT has suddenly been stopped (see Sec. IV B). This channeltron is operated at a sufficiently low voltage, such that the output current can safely be assumed to vary linearly with the detection rate.

## IV. RESULTS AND DISCUSSION

### A. MOT results

#### 1. Temporal fluctuations in the MOT

While observing the fluorescing cloud in real time with the CCD camera we noticed nonperiodic intensity fluctuations on a 50 ms timescale. Also, the cloud was irregularly 'breathing'. To determine the source of these fluctuations, we first took a series of ten pictures of the cloud. The shutter time for each picture was 1/60 s, and the elapsed time between two subsequent exposures about 5 s. Fitting the cloud size for each individual picture we obtain an average MOT volume with a standard deviation of 9%, while the temperature remained constant within 2.5%. According to Eqs. 1 and 3, this may be related to the unstable laser power. In that case the resulting density fluctuations should influence the rate at which ions are produced in two-body Penning collisions. To observe this, we compared the continuous ion signal with the laser intensity as a function of time. It turns out that the 4% laser intensity noise correlates to the ion signal noise, though it does not explain all irregularities in the ion signal. Using Eq. (3) we find that the measured intensity fluctuations may give rise to 6% variations in the deduced MOT volume.

#### 2. Atom number and density distribution

The maximum number of loaded atoms as derived from the fluorescence is  $2.5(3) \times 10^7$  at a detuning  $\Delta = -35$  MHz and gradient  $\partial B/\partial z = 39$  G/cm. The total intensity in this case is about  $100I_0$ . It is possible to run the MOT at intensities as low as  $40I_0$ , although the number of trapped atoms increases with intensity. To ensure a reliable estimate of the cloud dimensions and fluorescence intensity we take the average of five subsequent images. The uncertainty in the number of trapped atoms mainly arises from the inaccuracy of the value of the phenomenological constant  $C$  (8%), as well as from an error in the fluorescence measurement. The uncertainty in the fluorescence measurement is set by the 4% inaccuracy in the calibration and by the shot-to-shot fluctuations between the individual images used in the average. To ensure consistency between the results of the fluorescence and TOF measurement, we have to assign a value of 15(2)% to the detection efficiency of the channeltron. A Gaussian density function fits well to the cloud image. From the fit we infer the rms radii in the  $z$  and  $\rho$  dimensions and, thus, the volume  $V$ . At optimized trapped atom number, we find  $V = 0.020(5)$  cm<sup>3</sup>. By increasing the magnetic field gradient to  $\partial B/\partial z = 45$  G/cm, and decreasing the detuning to  $\Delta = -35$  MHz, the cloud was compressed to  $V = 0.0043(4)$  cm<sup>3</sup>. Still, it contained  $1.7(2) \times 10^7$  atoms.

Compared to a 1083 nm MOT, typical values for the

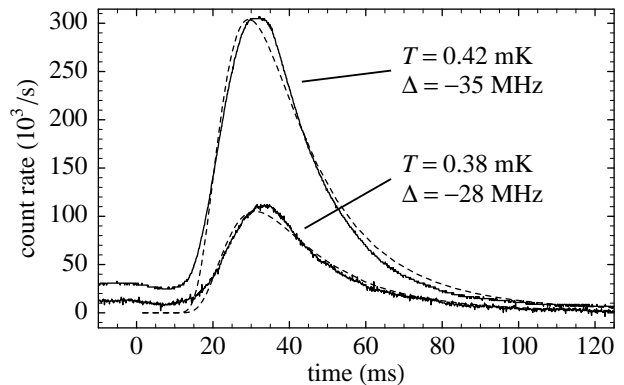


FIG. 4: Two typical TOF spectra (solid curves) and corresponding fits to the data (dashed curves), at detunings  $\Delta = -35$  MHz and  $\Delta = -28$  MHz, respectively. The nonzero offset at  $t \leq 0$  ms is ascribed to loss of metastables during loading of the MOT, due to imperfect alignment.

volume  $V$  of the 389 nm MOT are found to be 6 to 25 times smaller [5]. Although the auxiliary laser beam at 1083 nm acts as a seventh MOT beam, its effect on the cloud volume is negligible on account of its large detuning (80 MHz), and the relatively small photon momentum of the 1083 nm light. Using Eq. (1) and Eq. (3),  $V$  can be corrected for the different magnetic field gradients, saturation parameters, and temperatures for the 389 nm and 1083 nm cases. It follows that the observed compression of the cloud, due to only the increased laser cooling force, is approximately a factor 5, as predicted in Sec. II A. The optimum number of atoms is achieved with a relatively large magnetic field gradient, about twice as large as in a 1083 nm MOT.

With the knowledge of  $N$  and  $V$  we can determine the central density  $n_0 = N/V$ , which is  $1.4(5) \times 10^9$  cm<sup>-3</sup> in the case of optimized trapped atom number. The large error bar, indicating the spread about the mean of the central densities obtained from each picture, is probably due to the correlation between the volume and the 389 nm laser power fluctuations. A sudden increase in power leads to a smaller volume, while the fluorescence intensity increases, resulting in an overestimate of the trapped atom number. The aspect ratio  $\sigma_z/\sigma_\rho$  of the cloud turns out to be 0.96(2). We compared this with the aspect ratio as predicted by Eq. (1): since at equilibrium  $k_B T = \kappa_\rho \langle \rho^2 \rangle = \kappa_z \langle z^2 \rangle$ , with  $\kappa_\rho$  and  $\kappa_z$  the spring constants of the MOT in the radial and axial directions, respectively, it follows that  $\sqrt{\kappa_\rho/\kappa_z} = \sigma_z/\sigma_\rho$ , resulting in an aspect ratio of 0.79. This may indicate a small temperature difference between the  $\rho$ - and  $z$ -directions, also observed in a 1083 nm MOT [5].

#### 3. Temperature

Fitting a Maxwell-Boltzmann distribution function to the TOF spectra reveals the temperature  $T$  of the atoms

in the MOT (Fig. 4). The fit is not perfect and the deduced temperature may be somewhat overestimated. Furthermore, a nonzero offset at  $t \leq 0$  is observed which becomes more prominent (at the expense of trapped metastables) when the MOT laser beams are misaligned. The offset may also incorporate loss of metastables due to radiative escape [1], but our setup does not allow us to discriminate between different sources of hot metastables. Measured temperatures range from 0.46(1) mK for  $\Delta = -41$  MHz and  $S = 19$ , to 0.25(1) mK at  $\Delta = -9$  MHz and  $S = 15$ . In the latter case, however, the number of atoms in the MOT is limited to only  $2.2 \times 10^5$ . To our knowledge, these temperatures are significantly lower than any previously reported 1083 nm MOT temperature, and even surpass temperatures obtained in 1083 nm 3D-optical molasses applied to a large cloud of He\* atoms [5, 9, 10, 17, 18, 19].

Commonly, temperatures observed in a 1083 nm MOT are in good agreement with predictions given by the usual Doppler model [11]:

$$k_B T = -\frac{\hbar\Gamma}{4} \frac{1 + 2\mathcal{N}S + (2\delta)^2}{2\delta}. \quad (5)$$

Here,  $\mathcal{N}$  is the dimensionality of the molasses. When using Eq. (5) to calculate the 389 nm molasses temperature in order to test our results, two features that distinguish the 389 nm transition from the 1083 nm transition are relevant. First, the transition strength, determined by the Einstein coefficient  $A_{389} \equiv \Gamma_{389} = 2\pi \times 1.5$  MHz, is slightly less than for the 1083 nm transition ( $\Gamma_{1083} = 2\pi \times 1.6$  MHz) [7]. This decreases the 389 nm molasses temperature by 8% (here  $\Gamma_{389}$  should not be confused with the inverse lifetime:  $(\Gamma_{389})^{-1} = 106$  ns, whereas the lifetime of the  $3^3P$  state is 95 ns due to the presence of the extra  $3^3P \rightarrow 3^3S$  decay channel [7]). Second, the 10% decay via the  $3^3S_1$  cascade slightly reduces the diffusion, as the recoil of the photons involved is randomly distributed. A recalculation of the momentum diffusion constant for this case yields a 3% reduction. Thus, we expect the 389 nm molasses temperature to be 11% lower with respect to the 1083 nm case. Still, the predicted temperature is 1.1 mK for  $\Delta = -41$  MHz and  $S = 19$ , and 0.38 mK for  $\Delta = -9$  MHz and  $S = 15$ , appreciably higher than measured under the same circumstances.

The low temperatures found in our MOT may indicate that (sub-)Doppler cooling mechanisms are more efficient using the 389 nm transition. The sub-Doppler frictional force is indeed proportional to  $k^2$ . However, the sub-Doppler temperature limit (at low saturation parameter) is independent of  $k$ , as the diffusion coefficient also scales with  $k^2$ . Moreover, the capture velocity for such mechanisms is proportional to the wavelength of the transition and therefore smaller in the 389 nm case. Also, the recoil temperature associated with the absorption and emission of single 389 nm photons ( $32 \mu\text{K}$ ) is close to the Doppler limit ( $36 \mu\text{K}$ ), and therefore sub-Doppler cooling theory is expected to fail for the temperatures observed in our

MOT. At present, the efficiency of sub-Doppler mechanisms in 389 nm molasses compared to 1083 nm molasses remains an open question.

## B. Trap losses

The number of atoms  $N$  in the MOT is governed by the well-known rate equation

$$\frac{dN(t)}{dt} = L - \alpha N(t) - \beta \int n^2(\mathbf{r}, t) d^3r \quad (6)$$

where  $L$  denotes the loading rate, and  $\alpha$  and  $\beta$  are loss rate coefficients for processes involving one and two metastables, respectively. Accordingly, when the loading is interrupted the local density  $n$  changes in time following

$$\frac{dn}{dt} = -\alpha n - \beta n^2. \quad (7)$$

Assuming a Gaussian density profile characterized by a time-independent width, the losses can be expressed in terms of the central density  $n_0$  [20]:

$$\frac{dn_0(t)}{dt} = -\alpha n_0(t) - \frac{\beta}{2\sqrt{2}} n_0^2(t). \quad (8)$$

The losses are largely due to Penning-ionizing collisions, which yield one positively charged ion per loss event. These ions are attracted towards the ion detector, resulting in an ion flux  $\phi$ .

The loss rate constants are determined from the trap decay when the loading is stopped by simultaneously blocking all 1083 nm laser beams entering the apparatus. This disables the Zeeman slower and collimation section, and prevents the auxiliary Zeeman slower laser beam of contributing to the two-body collision rate via light-assisted collisions. Switching off the collimation minimizes the Penning ionization contribution of metastables from the atomic beam and, thus, reduces the background signal.

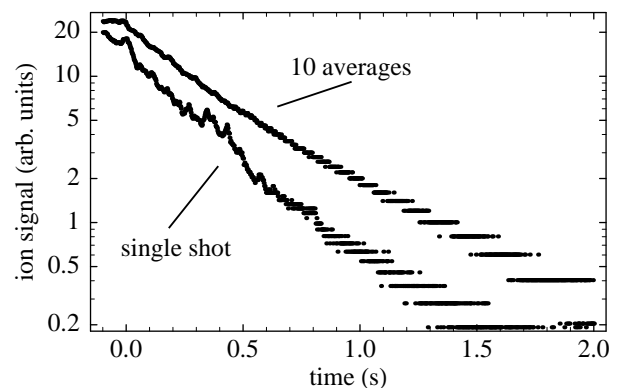


FIG. 5: Lower curve: typical nonexponential decay of the ion signal after the loading has been stopped at  $t = 0$  ms. Upper curve: ion signal obtained after averaging over 10 decay curves.

### 1. Collisional losses

The decay of the MOT is observed by recording the current  $\phi(t)$  from the ion-detecting channeltron [5, 20]:

$$\phi(t) = V \left( \epsilon_a \alpha n_0(t) + \frac{\epsilon_b \beta}{4\sqrt{2}} n_0^2(t) \right) + B. \quad (9)$$

Here,  $B$  is a constant background signal and  $\epsilon_a$  and  $\epsilon_b$  are the efficiencies with which ions are produced and detected for losses due to background and two-body collisions, respectively. Collisions that do not lead to Penning ionization but do result in trap loss, e.g. collisions with groundstate helium atoms, reduce  $\epsilon_a$ . Radiative escape may affect  $\epsilon_b$ . For the fit procedure, the ratio  $\epsilon = \epsilon_b/\epsilon_a$  must be known. From the increase in background pressure when the helium atomic beam is running, we deduce that the background gas consists for 80% of helium when the MOT is on. Unfortunately, our setup is not suited for experimental determination of  $\epsilon$ , as done by Bardou *et al.* [20]. They experimentally found  $\epsilon = 4 \pm 1$ . Since in our case the background gas involves mainly ground-state helium atoms, we expect  $\epsilon_a$  to be smaller than unity. The value of  $\epsilon_b$  is probably close to unity: following Tol *et al.* [5], one finds that for the 1083 nm case  $\epsilon_b \approx 0.98$ . We take the obvious underestimate  $\epsilon = 1$ , which implies that the result of the fit for  $\beta n_0$  has to be considered an upper limit. The result for  $\alpha$  can also be obtained by fitting the tail of the decaying ion signal, where the density is low enough to neglect the contribution of the two-body losses. In this way, the significance of  $\epsilon$  in the determination of  $\alpha$  is strongly (but not completely) reduced.

A typical example of a decaying ion signal is depicted in Fig. 5. The decay clearly shows nonexponential behavior, indicating that two-body collisions contribute significantly to the total losses. Since laser power fluctuations cause density fluctuations, much noise is visible in the ion signal. Therefore an average of ten decay transients is fitted, as also shown in Fig. 5. Unfortunately, this may affect the reliability of the fitted parameters as the two-body loss rate depends nonlinearly on intensity. However, apart from intensity noise the 389 nm output remained constant over a period sufficiently long to perform the measurements.

The fit procedure yields values for the exponential time constant  $\alpha$  and the nonexponential time constant  $\beta n_0$ . We typically find  $\alpha = 2 \text{ s}^{-1}$  and  $\beta n_0 = 3 \text{ s}^{-1}$ . This gives the rate coefficient  $\beta$  from the fit parameter  $\beta n_0$ , using  $n_0$  from the fluorescence measurement. We find  $\beta = 1.0(4) \times 10^{-9} \text{ cm}^3/\text{s}$ , at a detuning of  $-35 \text{ MHz}$ . Assuming a value  $\epsilon = 4$ , the result becomes  $\beta = 6(2) \times 10^{-10} \text{ cm}^3/\text{s}$ . The value  $\beta = 1.0(4) \times 10^{-9} \text{ cm}^3/\text{s}$ , which we interpret as the upper limit, is significantly below the value for the 1083 nm case of  $5.3(9) \times 10^{-9} \text{ cm}^3/\text{s}$ , reported by Tol *et al.* [5] using the same detuning and similar saturation.

The small value for  $\beta$  may be explained by a simple argument from cold-collision theory. A light-assisted

TABLE I: Comparison of the 389 nm MOT with the 1083 nm MOT described in Ref. [5]. The typical results for both MOTs are obtained under conditions that optimize both density and atom number. For the 389 nm case  $\epsilon = 1$  is assumed.

MOT wavelength	389 nm	1083 nm
Detuning $\Delta$ (MHz)	-35	-35
Magnetic field gradient $\partial B/\partial z$ (G/cm)	41	20
Total intensity ( $I_0$ )	100	90
Number of atoms $N$	$2 \times 10^7$	$5 \times 10^8$
Loading rate $L$ ( $\text{s}^{-1}$ )	$< 10^8$	$> 5 \times 10^9$
Central density $n_0$ ( $\text{cm}^{-3}$ )	$4 \times 10^9$	$4 \times 10^9$
Volume $V$ ( $\text{cm}^3$ )	0.005	0.12
Temperature $T$ (mK)	0.42	1.1
Two-body loss rate $\beta n_0$ ( $\text{s}^{-1}$ )	3	21
Two-body loss rate constant $\beta$ ( $\text{cm}^3/\text{s}$ )	$1.0(4) \times 10^{-9}$	$5.3(9) \times 10^{-9}$
Two-photon ionization loss rate constant $\alpha_{2ph}$ ( $\text{s}^{-1}$ )	0.5	0

collision can be regarded as two  $2^3S_1$  atoms that are resonantly excited to a molecular complex. For small detunings, this occurs at relatively large internuclear separation, where the molecular potential  $U$  is well-approximated by the dipole-dipole interaction

$$U_{\pm} = \pm \frac{C_3}{R^3}. \quad (10)$$

Here,  $R$  is the internuclear distance, and  $C_3 \simeq \hbar\Gamma(\lambda/2\pi)^3$  [1]. The excitation by the red-detuned MOT laser light takes place resonantly when the molecular potential energy compensates the detuning. This sets the so-called Condon radius  $R_C$ :

$$R_C = \left( \frac{C_3}{2\pi\hbar|\Delta|} \right)^{1/3}. \quad (11)$$

The red detuning selects an attractive molecular state. Once excited, the two atoms are accelerated towards small internuclear distances, where Penning ionization occurs with high probability. It follows from Eq. (10) and Eq. (11) that the Condon radius for 389 nm excitation is 2.8 times smaller than for 1083 nm. Classically, the cross section for the collision is determined by the square of the Condon radius, and is therefore expected to decrease by almost a factor 8.

To identify the role played by light-assisted collisions in the total two-body losses, we assume that  $\beta$ , as defined in Eq. (7), can be decomposed in two terms:  $\beta_{SS}$  and  $\beta_{SP}$ . Here  $\beta_{SS}$  is the rate coefficient for losses due to collisions between  $2^3S_1$  atoms in the absence of light, whereas  $\beta_{SP}$  takes the light-assisted collisional losses into account and depends (for given detuning and saturation parameter) on the cross section and, thus, on the Condon radius as described above. We neglect collisions between excited-state atoms, since the excited-state population in our far-red-detuned MOT does not exceed 0.01. We can define



$\beta_{SS}$  and  $\beta_{SP}$  also via Eq. (7), with the total density  $n$  replaced by the  $2^3S_1$  density  $n_S$ :

$$\frac{dn_S}{dt} = -\alpha n_S - (\beta_{SS} + \beta_{SP})n_S^2. \quad (12)$$

Since the excited-state population is small,  $n_S \approx n$ . It now follows immediately from Eq. (7) and Eq. (12) that to good approximation  $\beta = \beta_{SS} + \beta_{SP}$ .

$\beta_{SS}$  has been measured in a 1083 nm MOT by Tol *et al.* [5] to be  $\beta_{1083}^{SS} = 2.6(4) \times 10^{-10}$  cm<sup>3</sup>/s. Subtracting this from the total rate coefficient  $\beta_{1083} = 5.3(9) \times 10^{-9}$  cm<sup>3</sup>/s, we infer  $\beta_{1083}^{SP} = 5(1) \times 10^{-9}$  cm<sup>3</sup>/s, which is much larger than  $\beta_{1083}^{SS}$ . In contrast, the upper limit we find for  $\beta_{389}$  is of the same order of magnitude as  $\beta_{389}^{SS}$  (since 1083 nm and 389 nm magneto-optical traps, operated under the same conditions, are assumed to lead to similar populations of the  $2^3S_1$ ,  $M = -1, 0, 1$  levels, we can take  $\beta_{389}^{SS} = \beta_{1083}^{SS}$ ). To obtain the upper limit for  $\beta_{389}^{SP}$ , we subtract  $\beta_{389}^{SS}$  from  $\beta_{389}$  and find  $\beta_{389}^{SP} \leq 7(3) \times 10^{-10}$  cm<sup>3</sup>/s. This is in good agreement with the prediction following our simple argument. In addition to the upper limit found for  $\beta_{389}$ , we can now assign a lower limit equal to  $\beta_{389}^{SS} = 2.6(4) \times 10^{-10}$  cm<sup>3</sup>/s. Summarizing, we find  $2 \times 10^{-10}$  cm<sup>3</sup>/s  $< \beta_{389} < 1.0 \times 10^{-9}$  cm<sup>3</sup>/s.

## 2. Two-photon ionization

From the fit to the ion signal decay, we extract the linear loss rate coefficient  $\alpha$ . Unlike the situation in 1083 nm magneto-optical traps,  $\alpha$  is not solely determined by background-gas collisions, but also by the two-photon ionization rate. We assume that each loss event involves only one He\* atom and ignore photoionization of the molecular complex formed during a light-assisted collision, as this process enters Eq. (8) via  $\beta$ . Hence the loss rate coefficient can be written

$$\alpha = \alpha_{bgr} + \alpha_{2ph}, \quad (13)$$

where  $\alpha_{bgr}$  denotes the background gas collisional rate, and  $\alpha_{2ph}$  accounts for the two-photon ionization loss rate. Two processes can be thought to cause the ionization: two-photon ionization of a  $2^3S_1$  atom, or photoionization of an atom in either the  $3^3P_2$  or the  $3^3S_1$  state. The latter state is populated only during the cascade and has a lifetime of only 35 ns, so its contribution will be negligible. The instantaneous two-photon ionization probability  $p_{inst}$  is, for not too large detuning  $\Delta$ , dependent on intensity  $S$  and MOT detuning  $\Delta$  according to

$$p_{inst} \propto \frac{S^2}{\Delta^2}. \quad (14)$$

The photoionization probability  $p_{pi}$  of a helium atom in the  $3^3P_2$  state is simply proportional to the incident laser intensity and the cross-section for photoionization, which

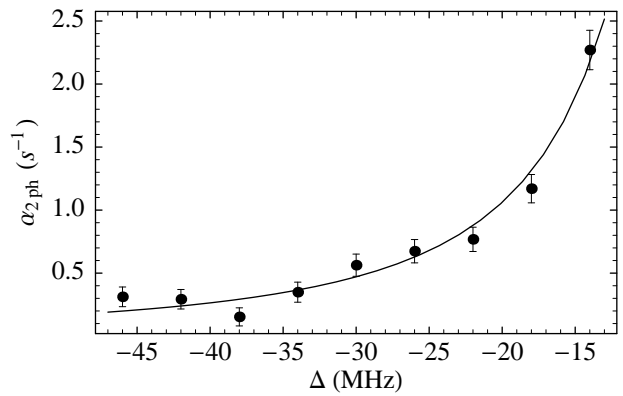


FIG. 6: Two-photon loss rate constant  $\alpha_{2ph}$  versus MOT detuning for total saturation parameter  $I_{total}/I_0 = 6S = 110$ .

varies only slowly with wavelength [21]. Neglecting this wavelength dependence, the probability of photoionization simply becomes the product of the upper  $3^3P_2$  state population and the ionization probability itself. For the two-step process, this leads to a dependence on intensity and detuning as

$$p_{pi} \propto \frac{S^2(\Gamma/2)^2}{\Delta^2 + (S+1)(\Gamma/2)^2}. \quad (15)$$

When  $\Delta^2 \gg (S+1)(\Gamma/2)^2$ , this dependence takes on a form similar to Eq. (14). We confirmed this behavior by measuring  $\alpha_{2ph}$  as a function of MOT detuning, as shown in Fig. 6. We also checked the intensity dependence, as shown in Fig. 7. In both cases we determined  $\alpha_{bgr}$  by measuring  $\alpha$  as a function of background pressure, while keeping the detuning and intensity fixed. Assuming a linear variation of  $\alpha_{bgr}$  with pressure, against a fixed background  $\alpha_{2ph}$ , a fit to the data points yields  $\alpha_{bgr} \approx 1.5(1)$  s<sup>-1</sup>. Under typical experimental conditions, we find  $\alpha_{2ph} \approx 0.5$  s<sup>-1</sup>.

Chang *et al.* calculated photoionization cross sections of many singlet and triplet states in helium, including the  $3^3S$  and  $3^3P$  states, for various wavelengths [21]. Using

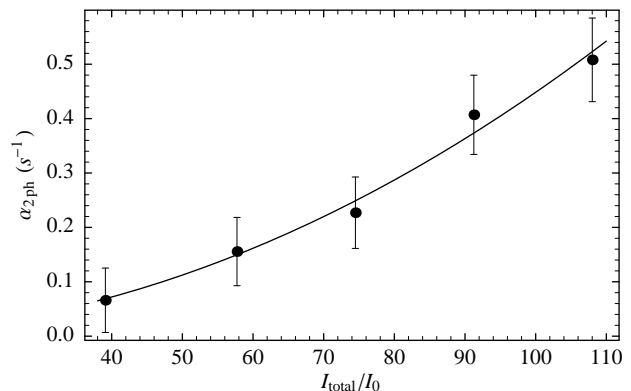


FIG. 7: Two-photon loss rate constant versus total saturation parameter  $I_{total}/I_0$  at a detuning  $\Delta = -35$  MHz.

their results we find photoionization rates of about  $2 \text{ s}^{-1}$ . Since the fraction of  $n = 3$  atoms in our MOT is typically below the 1% level, the net loss rate due to the two-step process then would be one order of magnitude smaller than the measured value for  $\alpha_{2ph}$ . This suggests that instantaneous two-photon ionization dominates over the two-step ionization losses.

### C. Auxiliary Zeeman slower, loading rate, and MOT capture velocity

To test the performance of the auxiliary Zeeman slower, we first optimized the number of atoms in the MOT in the absence of the extra slowing laser. Then, leaving the MOT parameters unaltered, we unblock the auxiliary laser beam and vary the slower laser intensities and Zeeman coil current iteratively until a new optimum for the number of atoms is established. Indeed, blocking the additional laser beam again interrupts the loading, demonstrating that we have tuned the end velocity of the Zeeman decelerator above the capture velocity of the MOT. With the auxiliary Zeeman slower on, the number of atoms is 40% times larger as compared to the case without the auxiliary Zeeman slower. Making use of Eq. (6), with  $\alpha$ ,  $\beta$ , and  $n_0$  known from experiment, we calculate that the auxiliary Zeeman slower enhances the loading rate by a factor 1.6. Despite this improvement, the loading rate remains low. By solving Eq. (6), with the measured values for the loss rate constants and the steady-state number of atoms as input, we find a loading rate slightly below  $10^8 \text{ s}^{-1}$ . Tol *et al.* [5] state a value of  $5 \times 10^9 \text{ s}^{-1}$  for their 1083 nm MOT. This difference is explained by the smaller MOT diameter, the reduced flux of slow atoms from the Zeeman slower due to atomic beam expansion, and imperfect collimation due to the relatively large bandwidth of the 1083 nm laser.

From the Zeeman slower settings it is possible to calculate the end velocity of the atoms and, thus, the capture velocity of the MOT. Therefore, the equations of motion of an atom subject to the decelerating laser beam are solved. We take into account the saturation parameter, the laser beam intensity profile, and the magnetic field (obtained from a detailed calculation). In this way we derive a capture velocity of 35 m/s (without using the auxiliary Zeeman slower). Apparently, the prediction of a 24 m/s capture velocity by the model of Sec. II B is an underestimate, and the true capture velocity lies closely to the velocity determined by the resonance condition. Therefore, it is likely that  $\pi$  and  $\sigma$  transitions, caused by MOT laser beams orthogonal to the quantization axis, occur at rates at least comparable to the 10% decay via the  $3^3S_1$  cascade. Apparently, the nonclosed character of the 389 nm transition plays a minor role, even in the case of relatively large ( $\sim 40 \text{ G}$ ) magnetic fields.

We derive from the settings of the Zeeman slower that atoms with a velocity of at most 75 m/s are further decelerated to a velocity of 35 m/s by the auxiliary Zeeman

slower. This translates to an increase in loading rate by a factor 1.7, in reasonable agreement with the result of the test described above.

### D. Comparison with 1083 nm MOT

Table I contains MOT results for the 389 nm and 1083 nm case [5]. Both MOTs have similar detuning and saturation parameter, which optimize both density and trapped atom number. The smaller number of atoms  $N$  in the 389 nm MOT is explained by the small loading rate. Despite this small number, the central density  $n_0$  is equal to that of a 1083 nm MOT containing over one order of magnitude more atoms. This is the result of the smaller loss rate constant  $\beta$ , the larger laser cooling force, and the larger magnetic field gradient. The latter not only contributes to the compression of the cloud, but also reflects the necessity of a large Zeeman detuning to compensate the larger Doppler shift of the atoms to be captured from the Zeeman-decelerated  $\text{He}^*$  beam. Furthermore, we observe that the  $0.5 \text{ s}^{-1}$  contribution of two-photon ionization to the losses in the 389 nm MOT is small compared to the  $21 \text{ s}^{-1}$  two-body loss rate in a large 1083 nm MOT.

## V. CONCLUSION AND OUTLOOK

We have shown that it is possible to build a magneto-optical trap using the 389 nm transition in triplet helium. Our prototype MOT demonstrates that a 389 nm MOT offers the advantage of a dense, cold cloud of metastable helium atoms, as compared to a 1083 nm MOT. The relatively large density is allowed by the reduced two-body loss rate coefficient  $\beta$ , whereas the large spontaneous force moderates substantial compression of the cloud. Intensity noise on the 389 nm output, however, compromises the measurement accuracy. Together with the high background pressure and the small value of  $\beta$ , this has complicated an accurate determination of its value. We conclude that  $\beta$  lies between the experimentally determined upper limit  $1.0 \times 10^{-9} \text{ cm}^3/\text{s}$ , and the two-body loss rate constant in the absence of light,  $2 \times 10^{-10} \text{ cm}^3/\text{s}$  determined in Ref. [5]. Two-photon ionization losses, although present, do not exclude the future possibility of a 389 nm MOT containing large numbers of metastable helium atoms at high phase-space density. To this end, however, the loading rate of the MOT must be improved. A bare 389 nm MOT has limited loading capabilities since the large Doppler shift implies a reduced capture velocity, and the required Zeeman slower settings then give rise to a smaller flux of slow metastables. The nonclosed character of the 389 nm transition, however, does not play an important role in the capture process, as well as in the other physics involved in the MOT.

For the near future we plan an ultimate experiment, in a configuration with a loading rate increased by two

orders of magnitude. To realize this, a 1083 nm MOT with  $\sim 30$  mm diameter laser beams will be overlapped with a  $\sim 10$  mm diameter 389 nm MOT. To avoid large two-body losses in the trapped cloud due to the presence of red-detuned 1083 nm light, a  $\sim 5$  mm diameter hole has to be created in the center of the 1083 nm MOT laser beams. This configuration will benefit from the superior loading capability of the 1083 nm MOT, as well as from the low-loss 389 nm environment containing a dense cloud at relatively low temperature. Furthermore, we will test the effectiveness of 389 nm molasses on a metastable helium cloud, precooled by a 1083 nm MOT. This seems promising not only because of the low temperatures observed already in our 389 nm MOT, but also because of the relatively high saturation intensity. This can be seen as follows. In a 1083 nm molasses, starting with a large, dense cloud of helium metastables, the relative absorption is rather large [10]. Within the cloud,

this results in intensity imbalances between two counter-propagating molasses laser beams, and these imbalances are believed to reduce the effectiveness of the molasses. The larger saturation intensity of the 389 nm transition implies lower relative absorption and, thus, a reduced intensity imbalance. Therefore, we expect to obtain lower temperatures in a 389 nm molasses.

## VI. ACKNOWLEDGEMENTS

We are indebted to J. Bouma for his contribution to the design and construction of the setup. We thank P.J.J. Tol and N. Herschbach for stimulating discussions. The Space Research Organization Netherlands (SRON) is gratefully acknowledged for financial support.

- 
- [1] J. Weiner, V. S. Bagnato, S. Zilio, and P. S. Julienne, *Rev. Mod. Phys.* **71**, 1 (1999).
- [2] M. H. Anderson, J. R. Ensher, M. R. Matthews, C. E. Wieman, and E. A. Cornell, *Science* **269**, 198 (1995).
- [3] A. Robert, O. Sirjean, A. Browaeys, J. Poupard, S. Nowak, D. Boiron, C. I. Westbrook, and A. Aspect, *Science* **292**, 461 (2001).
- [4] F. Pereira Dos Santos, J. Léonard, Junmin Wang, C. J. Barrelet, F. Perales, E. Rasel, C. S. Unnikrishnan, M. Leduc, and C. Cohen-Tannoudji, *Phys. Rev. Lett.* **86**, 3459 (2001).
- [5] P. J. J. Tol, N. Herschbach, E. A. Hessels, W. Hogervorst, and W. Vassen, *Phys. Rev. A* **60**, R761 (1999).
- [6] R. Schumann, C. Schubert, U. Eichmann, R. Jung, and G. von Oppen, *Phys. Rev. A* **59**, 2120 (1999).
- [7] G. W. F. Drake, ed., *Atomic, Molecular, & Optical Physics Handbook* (AIP Press, 1996).
- [8] H. J. Metcalf and P. van der Straten, *Laser Cooling and Trapping* (Springer-Verlag New York, 1999).
- [9] A. Browaeys, J. Poupard, A. Robert, S. Nowak, W. Rooijakkers, E. Arimondo, L. Marcassa, D. Boiron, C. I. Westbrook, and A. Aspect, *Eur. Phys. J. D* **8**, 199 (2000).
- [10] F. Pereira Dos Santos, J. Léonard, Junmin Wang, C. J. Barrelet, F. Perales, E. Rasel, C. Unnikrishnan, M. Leduc, and C. Cohen-Tannoudji, *Eur. Phys. J. D* **19**, 103 (2002).
- [11] P. D. Lett, W. D. Phillips, S. L. Rolston, C. E. Tanner, R. N. Watts, and C. I. Westbrook, *J. Opt. Soc. Am. B* **6**, 2084 (1989).
- [12] K. Sengstock and W. Ertmer, *Adv. At. Mol. Opt. Phys.* **35**, 1 (1995).
- [13] V. S. Lethokov and V. G. Minogin, *Phys. Rep.* **73**, 1 (1981).
- [14] W. Rooijakkers, W. Hogervorst, and W. Vassen, *Opt. Comm.* **123**, 321 (1996).
- [15] Throughout this paper, presented uncertainties and noise levels correspond to one standard deviation.
- [16] C. G. Townsend, N. H. Edwards, C. J. Cooper, K. P. Zetie, C. J. Foot, A. M. Steane, P. Szafrtger, H. Perrin, and J. Dalibard, *Phys. Rev. A* **52**, 1423 (1995).
- [17] M. Kumakura and N. Morita, *Phys. Rev. Lett.* **82**, 2848 (1999).
- [18] H. C. Mastwijk, J. W. Thomsen, P. van der Straten, and A. Niehaus, *Phys. Rev. Lett.* **80**, 5516 (1998).
- [19] D. V. J. Milic, Ph.D. thesis, Australian National University, Canberra (1999).
- [20] F. Bardou, O. Emile, J. M. Courty, C. I. Westbrook, and A. Aspect, *Europhys. Lett.* **20**, 681 (1992).
- [21] T. N. Chang and T. K. Fang, *Phys. Rev. A* **52**, 2638 (1995).